PCCP

Accepted Manuscript

ROYAL SOCIETY OF CHEMISTRY

www.rsc.org/pccp

Carrier concentration dependent optical and electrical properties of Ga doped ZnO hexagonal nanocrystals

Manas Saha, Sirshendu Ghosh, Vishal Dev Ashok and S. K. De*

Department of Materials Science, Indian Association for the Cultivation of Science, Jadavpur, Kolkata – 700032, INDIA

***E-mail: msskd@iacs.res.in**

Abstract:

Colloidal trivalent gallium (Ga) doped zinc oxide (ZnO) hexagonal nanocrystals have been prepared to introduce more carrier concentration into wide band gap ZnO. The dopant (Ga) modifies morphology and size of ZnO nanocrystals. Low content of Ga enhances optical band gap of ZnO due to excess carrier concentration in the conduction band of ZnO. The interaction among free carriers arising from higher concentration of Ga gives rise to narrowing of band gap. Surface plasmon resonance absorption appears in the infrared region due to excessive carrier concentration. Broad emission band consists of blue, yellow and green colors associated with different native defects of ZnO. Intrinsic defect and extrinsic dopant Ga control the defect related emission spectrum in the visible region. Replacement of Zn by Ga induces room temperature metallic state in degenerate semiconductor. Cationic disorder leads to metal –semiconductor transition at low temperature strongly dependent on the concentration of Ga. Pure semiconducting behavior up to about 80 K is observed for the highest amount of Ga. Temperature dependent metal - semiconductor transition has been interpreted by localization of charge carriers due to disorder arising from random Ga substitution.

Introduction:

The carrier concentration is a key and basic parameter to tune optical and electrical properties of metal and semiconductor. The collective oscillation of free electrons in metals leads to plasmon effect on the surface of metals. The frequency of oscillation depends on the concentration of free electrons and the dielectric constant of metal. The interaction of light with high dense electron gives rise to absorption due to plasmonic phenomenon. The optical absorption frequency can be easily varied from the ultraviolet (UV) to far-infrared (FIR) region through the reduction of size of metals[1]. High electrical conductivity of metal limits the plasmonic resonance application due to high absorption loss. Low loss plasmonic materials are very attractive because of development of new technology such as photothermal therapy, surface plasmon resonance sensor, plasmon enhanced fluorescence and solar cell. It is found that doped semiconductor nanocrystals reveal plasmonic effect in near infrared (NIR) region through the introduction of more carrier concentration in the conduction band of wide band gap semiconductor[2,3]. Cation and anion vacancies and doping by suitable atoms enhance the carrier concentration of semiconductor. Wide band gap semiconductors possess high optical transparency in the visible region and can have high electrical conductivity due to excess charge carrier in conduction band. Thus heavily doped semiconductors with large band gap may have the combined property of high optical transparency, good electrical conductivity and moderate plasmonic absorption.

The carrier concentration significantly influences the electronic energy band structure of large band gap semiconductor. The reconstruction and occupation of conduction band depends on the electronic states of the dopant ion and the free charge density of host semiconductor. The carrier concentration above the critical Mott carrier density results in increase of optical band gap

and semiconductor-metal transition at ambient condition. The widening of band gap increases the material optical transparency and the appearance of Fermi level in conduction band enhances electrical conductivity with additional carrier concentration. Zinc oxide (ZnO) is a very promising direct wide band gap semiconductor for innovative applications in electronic and optoelectronic devices[4,5]. In ZnO n-type doping naturally occurs due to native defects such as predominant oxygen vacancy due to the lowest formation energy during synthesis [6-9,10-12]. All possible types of vacancies and interstitial defects make ZnO the most attractive due to easily controllable the relative concentration of various defects and tunable electronic properties. The spontaneous formation of high density vacancy and defect in ZnO generates carrier concentration of $10^{18} - 10^{19}$ cm^{-3} very close to Mott critical carrier density[13-14]. The additional charge carrier created by impurities may significantly affect optical and electrical properties of ZnO. The valence electrons of group III elements have comparatively higher energy states and strongly hybridize with conduction band states of oxide semiconductors[15]. The group III elements (Al, Ga, In) can easily be doped into ZnO to generate free electrons which can fill up the conduction band levels to convert into degenerate semiconductor[10,16]. The isovalent group III elements have strong chemical effect which drives different phenomena depending on the interaction between dopant and host semiconductor. An intense experimental and theoretical investigation on aluminum doped ZnO indicates an enhancement of electrical conductivity and optical transparency up to about 3% Al substitution at Zn sites[17,18]. An anomalous change in Fermi level and resistance of ZnO depending on Al concentration has been predicted[13,19,20]. The surface plasmon absorption in the IR region has been tuned with Al concentration[21]. The incorporation of indium into ZnO lattice improves electrical conductivity and induces surface plasmon absorption in IR region[22-23]. The most important fact is that Ga (Z = 31) element is next to Zn (Z

= 30) element in the periodic table. As a result of it, the covalent bond length of Ga-O (1.92 Å) is comparable to that of Zn-O (1.97 Å). Effects of Ga doping on optical and electrical properties of ZnO thin films grown by various methods such as molecular beam epitaxy and pulsed laser deposition technique have been reported[24-26].

Nanocrystals are more advantageous due to large surface area than thin films. Moreover nanocrystals can be synthesized chemically with lower cost than thin film deposition by conventional physical methods. Size and morphology dependent properties of nonoscale semiconductors can easily be tuned by controlling the synthesis condition. The dopants generally diffuse to the surface of nanocrystals due to internal strain and self-purification[27]. It has been established that the dopants can introduce free carriers into nanocrystals only when dopants occupy interior substitutional sites of pristine lattice[28,29]. Hence inclusion of impurities in semiconductor nanostructures is a challenging task but it improves the physicochemical properties in comparison with bulk semiconductors. Recently, Ga doped ZnO spherical nanoparticles have been synthesized[30-32]. The most attractive fundamental property of ZnO in comparison with other wide band gap oxides is strong anisotropy along different crystallographic directions. Among a number of ZnO based morphologies, hexagonal pyramid is very rare. Hexagonal pyramid is superior to other common morphologies due to the existence of multiple facets. We report here optical and electrical properties of Ga doped ZnO hexagonal nanopyramids with systematic variation of Ga concentration.

Experimental Section:

Materials: Zinc Stearate [$Zn(St)_2$], Gallium (III) 2,4-pentanedionate, 99.99% (metal basis) [$Ga(acac)_3$] and 1-octadecene (ODE, 90%) were purchased from Alfa Aesar. Oleylamine

[(OLAM) 70%, tech] and Oleic acid (OLAC, 99%) were purchased from Aldrich. Formic acid (GR), Ethyl alcohol (GR), n-Hexane (GR) and Acetone (GR) were purchased from Merck. All chemicals were used as received.

Synthesis of Nano Crystals: In our synthesis protocol we took 1 mmole of $Zn(St)_2$ and 10 ml ODE in a 25 ml three neck round bottom flux fitted with reflux condenser. The mixture was heated to 120°C under vacuum and kept for 1 hr. There after the reaction was carried out under nitrogen atmosphere. The transparent yellow color solution was heated to 280° C rapidly at a heating rate 10°C/min. The reaction mixture was kept at 280°C for 30 min. 8 mmole OLAM and 5 ml ODE was degassed at room temperature in another round bottom flask and heated at 100 °C for 1 hr in constant evacuation to remove dissolved water. This transparent mixture was heated to 220 °C temperature in N_2 atmosphere. The hot mixture of ODE and OLAM was injected into $ZnSt_2$ solution in ODE heated at 280 °C. We continued the reaction for 8-10 min at 250 °C. The reaction mixture was cooled to room temperature and the product was precipitated by addition of 5 ml hexane and 30 ml ethanol. The product was collected by centrifuging the precipitate and washing was carried out for several times to remove impurities.

Keeping all the synthesis conditions similar, doped nanocrystals were prepared by varying the concentration of Ga [$Ga(acac)_3$] source in the solution such that the stoichiometric ratio of $Zn_{1-x}Ga_xO$ is maintained, where x = 0.0025, 0.005, 0.01, 0.02 and 0.04.

Characterization:

The content of Ga in ZnO was determined from the elemental analysis using atomic absorption spectroscopy (AAS) Shimadzu AA-6300 atomic absorption spectrophotometer. The crystalline phases of the products were determined by X-ray powder diffraction (XRD) by using

Bruker AXS D8SWAX diffractometer with Cu K_α radiation (λ= 1.54 Å), employing a scanning rate of 0.5° S^{-1} in the 2θ range from 20° to 80°. For XRD measurement the hexane solution of the NCs was drop cast over amorphous silicon sample holder till a naked eye visible thin layer was formed. Transmission electron microscopy (TEM) images, high angle annular dark field scanning TEM (HAADF STEM) images and energy dispersive spectrum (EDS) were taken using an Ultra-high resolution field emission gun transmission electron microscope (UHR-FEG TEM, JEM-2100F, Jeol, Japan) operating at 200 kV. For the TEM observations, the sample dissolved in hexane was drop cast on a carbon coated copper grid. The morphologies of the samples and film thickness were studied by a field emission scanning electron microscope (FESEM, JEOL, JSM 6700F). The room temperature optical absorbance of the samples was recorded by a Varian Cary5000 UV-VIS-NIR spectrophotometer. Photoluminescence (PL) measurements were carried out at room temperature with a Fluorescence spectrometer (Hitachi, F-2500). The luminescence decay curves were obtained by time correlated single-photon counting (TCSPC, HORIBA JOBIN YVON IBH) via time-to-amplitude conversion (TAC). The samples were excited at wavelength using LED (HORIBA JOBIN YVON IBH Nanoled-340) at a repetition rate of 1 MHz.

Thin film preparation and measurement:

A 2x2 cm^2 quartz substrate first clean with piranha solution for 10 mins. was used for thin film preparation. Then it was cautiously washed with de-ionized (DI) water and dried in 120° C in N_2 atmosphere for 4 hr. Then total 0.2 ml of nanocrystal solution in n-hexane (30 mg. ml^{-1}) was spin cast on clean quartz substrate at a speed of 700-900 rpm for 60 sec. and dry it for 30 min. in vacuum. After that the film was immersed in formic acid solution in acetonitrile for 5-8 min. to remove long chain capping agent. Then the film was annealed in Ar atmosphere for 4

hr. at 350-400 $^{\circ}$ C .To make Ohomic contact, Al electrode was deposited on two ends of film. Using silver paste, electrical connection was made on Al electrode. Sheet resistance as a function of temperature was measured in lab made cryostat with the help of liquid nitrogen, Keithley Electrometer 6517A and Lakeshore temperature controller model 332 in temperature interval 300 K to 80 K.

Results and Discussion:

The actual content of Ga for different samples is shown in Table 1. The crystalline phase and incorporation of Ga into ZnO has been confirmed from XRD as shown in Fig.1. In XRD patterns all the peak positions correspond to the hexagonal würtzite structure of ZnO (JCPDS No. 36-1451) which belongs to space group ($P6_{3mc}$). No significant unnatural XRD peaks are observed in doped samples due to other possible oxide based crystalline impurities such as β-Ga_2O_3[33] or mixed oxide ($ZnGa_2O_4$)[34]. This implies that the trivalent Ga^{3+} is properly doped in ZnO system. In doped system it has been observed that the peaks are broadened with increase of Ga loading. This effect might be due to the variation in shape or size of nanocrystals and also for the generation of lattice strain for the presence of dopant ions at the lattice site or in the interstitial site during the time of nanocrystals formation. In close observation, the most intense diffraction peaks viz: (100), (002) and (101) are shifted to higher angle (2θ), i.e. the spaces of crystallographic lattice plane decrease with increase of dopant mole%. The ionic radius of trivalent Ga^{3+} (0.062 nm) is much smaller than that of divalent Zn^{2+} (0.074 nm). This causes the shifting of diffraction peaks to higher angle in order to satisfy Bragg's law.

Rietveld refinements of the X ray diffraction for pure and doped samples were carried out using software MAUD (http://www.ing.unitn.it/~maud/) to estimate the lattice parameters (a and

c), crystal volume and lattice strain, shown in Fig. S1. Due to the smaller ionic radius of dopant Ga^{3+} it is observed that the lattice parameters a, c and volume of the crystal decrease with increasing Ga mole% in ZnO nanocrystals. Fig.S2 shows the compression of lattice parameter with Ga concentration. It is also observed that the compressive strain increases with higher doping percentage of Ga^{3+} shown in Fig.S3. It is observed that non linear decrease of lattice parameters a and c. The variation in the strain and lattice parameters may be attributed to size variation of nanocrystals and interstitial doping. Unit cell volume (V) was calculated from following equation[35]

$$V = 0.866 \times a^2 \times c \qquad (1)$$

It is observed that volume of unit cell varies from 51.94 A^3 to 45.67 A^3 with increase of Ga %.

Fig. 2a shows the TEM image of as-synthesized monodispersed ZnO nanocrystals. The figure depicts the well defined structure of ZnO as incomplete hexagonal-nanopyramids. The inset of Fig. 2a shows the tilted view of NCs and the thickness of NCs was found to be 15 - 19 nm. Fig. 2b shows HAADF-STEM image of incomplete nanopyramid. The size of nanocrystals was found to be 35 ± 1 nm at base and thickness of nanocrystals was 19 ± 1.5 nm. The good ring patterns from electron diffraction pattern were indexed to the hexagonal würzite structure (Fig. 2c), which is consistent with the XRD data. Fig. 2d shows the HRTEM image of single nanocrystal which shows a perfect hexagonal base of pyramid with each site of 21 nm in length. The würzite structured ZnO crystal consists of alternating planes composed of fourfold tetrahedrally coordinated Zn^{2+} and O^{2-} ions, staking alternatively along the c-axis. So the Zn^{2+} rich positive charged (0001) and O^{2-} rich negative charge $(000\bar{1})$ polar surfaces generate a permanent dipole along the c-axis[36]. Most of the ZnO nanostructures show preferential growth

along the c-axis for this inherent dipole moment. The FFT pattern in Fig. 2e is taken from the brown square area of nanocrystal in Fig. 2d (the cross section of two basal edges). From the circled spot in the FFT, the assigned planes are found to be $(11\bar{2}0)$, $(\bar{1}2\bar{1}0)$ and $(10\bar{1}0)$. The reconstructed TEM image from the FFT spots in Fig. 2f are consistent with the above mentioned planes. The surface was terminated by $(11\bar{2}0)$ group of planes and the $(10\bar{1}0)$ planes are parallel to basal edges. The polar $\{10\bar{1}1\}$ is the most exposed surface in the as-synthesized nanocrystals and there is no trace of thermodynamically stable facets like non-polar $\{10\bar{1}0\}$ and $\{2\bar{1}\bar{1}0\}$ which is very common in ZnO nanostructure system[37,38]. The six polar $\{10\bar{1}1\}$ facets make nearly 59º angle with basal edges. In this in-complete pyramid system most exposed facets are $\{0001\}$, $\{000\bar{1}\}$ and $\{10\bar{1}1\}$ and they are polar either Zn rich or O rich. So the kinetic control of the reaction here plays a vital role to stabilize unstable polar facets over thermodynamically stable non-polar facets. Oleylamine acting as both accelerating and capping agents plays a crucial role to determine ultimate morphology of the nanocrystals. The polar head of amine ($-NH_2$) and electron donating nature of amine stabilize the polar facets by electrostatic interaction and co-ordination with Zn-rich surfaces. Fig. 3 shows the HAADF-STEM image of x=0.01 doped ZnO nanocrystals which also show the incomplete nanopyramid morphology with decreased crystallite size. Energy dispersive X-ray spectroscopy (EDS) element mapping was performed to determine the exact position and distribution of dopant ions in the NCs. The EDS element mapping over large number of NCs shows that Ga^{3+} ions are homogeneously distributed among the NCs. No phase separation or agglomeration was noticed which conclude that the dopant distribution is quite good. Other two elements Zn and O were also present in nearly stoichiometric ratio and in well distribution. EDS line scan over a single nanocrystal also shows nearly homogeneous distribution of Ga^{3+} in a single nanoparticle shown in Fig. S4.

Fig. 4a shows the TEM image for x=0.02 Ga doped ZnO nanocrystals. The morphology and size of NC are drastically changed. The morphology changes from nanopyramid to inhomogeneous shaped hexagonal nanocrystals. Also the size decreases to 18 ± 3 nm from 35 nm for pure ZnO nanocrystals. This implies that the growth of nanocrystals was inhibited in the presence of Ga^{3+} ions. Incorporation of Ga^{3+} in ZnO crystal lattice increases the surface charge density of Zn rich polar surfaces, i.e.; Zn-{0001} and Zn-$\{10\bar{1}1\}$ surfaces due to higher electronegativity of Ga^{3+} than Zn^{2+}. This accretion of surface polarity favors faster electrostatic interaction and consequent surface stabilization or capping by OLAM onto the Zn-{0001} and Zn-$\{10\bar{1}1\}$ surfaces. More Ga^{3+} loading leads to more charge accumulation on above described surfaces which results in quenching of growth along the c-axis (decrease in pyramid height) and less exposure of $\{10\bar{1}1\}$ surfaces. In presence of excess Ga^{3+} x=0.04 the morphology of NCs was totally changed. Fig 4c shows the TEM image of x=0.04 Ga doped ZnO which depicts the presence of some flower like morphology. The average size of nanocrystals increases to 40-50 nm. The closer view of a nanoflower is highlighted in TEM image. Fig 4d clearly indicates the self-attachment of the NCs where the central NCs has size ~ 27 nm and outer six NCs ~ 20 nm. Somewhat the size is very close to the size of freestanding x=0.02 Ga doped ZnO NCs. The formation of nanoflower structure can be explained by the "oriented attachment process"[39] .

Decrease of crystallite size upon doping can be explained by Gibbs-Thomson relationship[40] .

$$S_r = S_B \exp[2\sigma V_m / rRT] \quad (2)$$

Where S_r is the solubility of the crystallite of radius r, S_B is the solubility of the corresponding bulk material, V_m is the molar volume, and σ is the specific surface energy of

nanocrystals. The compressive strain increases continuously with increase of the Ga concentration which in turn elevate specific surface energy, σ. Equation (2) suggests that larger strain induces greater crystallite solubility. As a result Ga dopants inhibit the growth of ZnO crystals and yield smaller particles than the pure one.

The oriented attachment process in the colloidal system occurs due to the 'Limited Ligand protection' of the nanocrystals. Oleylamine, free stearic acid (generated from zinc stearate) were believed to be the surface capping agent in the as-synthesized nanocrystals. When excess (x = 0.04) Ga was introduced in the system it also incorporate excess acetylacetonate ligand coming from the precursor. The acetylacetonate being a harder base than stearate or OLAM might absorb at the surface much faster than the OLAM, which leads to the improper surface protection[41,42]. Also the surface doping (as the NCs always try to expel the dopant ion by self purification process) of higher valent Ga^{3+} creates a local dipole moment and results in an increase of van der waals type of interaction (dipole-induced dipole, induced dipole-induced dipole). Both the factor leads to the easy coalescence of the nanocrystals maintaining the similar crystallographic alignment of the polar planes.

Introduction of Ga^{3+} into the ZnO lattice is expected to modify the energy band structure of ZnO nanocrystals which affects the optical properties of ZnO NCs. To access the exact effect and possible applications, we performed both the absorption and emission spectrum measurements. Fig. 5a shows the absorption spectra of all sample dissolved in carbon tetrachloride in the wave length region of 300 nm to 3300 nm. One absorption peak is observed for pure sample and two different absorption peaks are found for doped samples. The absorption peak around 362 - 372 nm. (in UV region) has shown in inset of Fig. 5a due to the band gap absorption. In infrared (IR) region absorption band is related to the localized surface plasmon

resonance (LSPRs) absorption. Surface plasmon resonance occurs due to the introduction of free carriers in doped nanocrystals, either by aliovalent cation doping or ionic vacancies. With the increasing of Ga content up to x=0.02 the plasmonic absorption increases monotonically but plasmonic absorption intensity decreases for higher value of x=0.04 which may be for destruction of particle size distribution, inhomogeneous doping and for electron trapping around Ga^{3+} ion[43]. Termination wavelength of UV-VIS-NIR instrument is 3300 nm, so we carried out FTIR spectroscopy to get the full nature of LSPRs band showed in fig. 5(b). The normalized absorbance peak position shifts towards higher frequency with raising Ga content i.e. the carrier concentration in ZnO nanocrystal increases with Ga^{3+} substitution.

The LSPRs frequency strongly depends on carrier concentration and carrier mobility. The modified Drude –Lorentz model can explain LSPRs absorption. The absorption coefficient (α) of the excess electrons in conduction band of semiconductor is given as follows:[44]

$$\alpha = \frac{e^2 N}{m^* \varepsilon_0 n c \gamma \omega^2} \quad (3)$$

Where e is electronic charge, N is the carrier concentration, c is the speed of light and ω is the frequency of light, m^* is the effective mass of electron, ε_0 the vacuum permittivity, n is the refractive index of pure semiconductor, γ is the mean time between two electron scattering event. LSPRs band absorption frequency based on Mie's theory is expressed as[3] :

$$\omega_p = \sqrt{\frac{Ne^2}{m^* \varepsilon_{opt} \varepsilon_0}} \quad (4)$$

ε_{opt} is the dielectric constant of semiconductor material measured in transparent region of spectrum. From equation (4) free carrier density in doped sample with parameters $m^* = 0.29m_0$[45-46], ε_{0pt}=7.77[47] (for bulk ZnO system) has been calculated and depicted in Table 2. The carrier

concentration was found to be of the order of 10^{19} cm^{-3} and increasing with increase in the concentration of Ga source in the precursor till x=0.02. On further increase in Ga concentration the value was found to decrease.

The absorption peaks in UV region are related to energy band gap. Optical band gap can be found from the differential absorption spectra $\frac{dA}{d\lambda}$ in Fig. S5[48]. Band gap energy increases with increase of dopant concentration . The band gap energy of pure and doped sample is presented in Table 2. Here the size effect of nanoparticle is not so important for band gap enhancing because particle size of doped samples are much bigger than exciton Bohr radius (2.1 nm.) for which quantum confinement effect is important. The blue shift of optical band gap can be attributed to the increase of Ga concentration, which creates free carriers in the host ZnO. The excess electrons occupy the lowest states in the conduction band and enhance the effective band gap. This behavior is called Burstein-Moss (BM) effect[14,49-50]. Increase of Fermi level in conduction band due to BM effect is responsible for energy band gap widening. The value of carrier concentration (N) is also determined from the shift of band gap due to BM effect and is presented in Table 2. The value of N calculated using BM effect is similar to using Mie's theory, Eq. (4). The difference in pre-factor is due to dielectric constant of solvent which is not accounted in BM effect. Comparison of carrier concentration using Mie's and BM effect it confirms that our doping process is homogenous. According to BM effect, band gap should increases with increase of Ga content. After certain limit of Ga concentration, band gap of sample starts to reduce[13,16,51]. The exchange and Coulomb interactions among the free carriers in the conduction band and carrier-impurity scattering leads to a downward shift of conduction band and upward shift of valence band[52]. So a renormalization of band gap occurs due to many

body effect, such as electron-electron, electron-ion, hole-ion, hole-hole which causes narrowing in the optical band gap of sample.

To know more about the change of optical properties and defects state upon Ga^{3+} doping in ZnO matrix steady state photoluminescence (PL) spectroscopy was performed. Fig. 6 shows the PL profile of pure and doped ZnO nanocrystals. Upon band gap excitation at 340 nm, all the nanocrystals show two types of emission: near band edge emission (NBE) in UV region and defect level emission (DLE) in the visible region. The NBE emission appeared at 378 nm - 385 nm upon photoexcitation of the NCs can be attributed to the radiative recombination of the photoexcited electron in the conduction band with the photo generated hole in the valence band. The DLE band is very broad (400 nm – 600 nm) compared to narrow NBE band (350 nm – 400 nm). The broad emission band is deconvoluted based on Gaussian distribution as depicted in Fig. 7 to extract the characteristic transitions of excited electrons to ground state levels. Each emission spectrum consists of a single broad peak in wavelength interval of 400-650 nm. The intensity difference between minima of each peak is small compared to peak intensity. In the deconvolution process, the base line of each spectrum was approximated linear with wavelength.

The wide DLE spectrum for pure ZnO is resolved into three well defined emission peaks centered at 465, 500 and 540 nm respectively. Green peak at 500 nm has the highest integrated intensity among three peaks. The lowest Ga doped sample (x = 0.0025) reveals a prominent peak at 420 nm corresponding to blue emission as distinctly indicated in Fig. 7(b). All the emission peaks as displayed in Fig. 7 are red shifted with increase of Ga concentration. The Ga doped ZnO nanocrystals for x = 0.01, 0.02, 0.04 show a broad yellow emission centered at 578 to 581 nm along with green emission. Integrated intensity of yellow emission increases concomitant with decrease of green emission.

The intermediate impurity levels within band gap region generated by defects determine the emission features of large band gap semiconductor. Physics and chemistry of defect formation and variation of defect concentration in ZnO are very complex[53]. Most of the vacant tetrahedral and octahedral lattice sites of relatively open crystal structure of ZnO favor both intrinsic and extrinsic interstitial defects. Different types of defects in ZnO nanocrystals create some localized donor states like shallow trap states near the conduction band and acceptor states or deep trap states near the valence band. Interstitial Zn ion (Zn_i) and oxygen vacancy (V_0) are the most common donor states in n-type ZnO[10,54-55]. The Zn_i and V_o in crystals give rise to shallow and deep donor levels within band gap. Zinc vacancy (V_{Zn}), interstitial oxygen (O_i) and oxygen atom at Zn lattice site (O_{Zn}) are the common acceptor states in ZnO system. The dopant Ga influences intrinsic defect states of ZnO significantly. Experimentally and theoretically it is found that Ga induces V_{Zn} in ZnO crystals due to self-charge compensation[56]. Moreover, Ga can also occupy both substitutional (Ga_{Zn}) and interstitial sites (Ga_i) of ZnO lattice[57]. For larger Ga concentration, vacancy complexes such as $Ga_{Zn} - V_{Zn}$ and $Ga_{Zn} - O_i$ are formed due to strong Coulomb interaction. These complexes affect mainly deep acceptor states. A large variety of defect levels control the emission bands in the visible region due to multiple transitions depending on available states of each defect level.

From pure ZnO, x = 0.0 to doped x = 0.02 NCs the relative intensity of DLE to the NBE gradually increases. These results from the higher probable of occurrence of recombination of electron with the deep trapped state rather than NBE states. This may be a result from the increased number of defect population upon Ga doping. Shallow donor levels and splitting of valence band (VB) due to strong crystal field and spin-orbit effects lead to large width of NBE. Blue emission band can be attributed to the formation of some Zn_i states which is closely

situated with the conduction band (CB) minimum. Recombination of electron from Zn_i states to VB results in blue emission[58-59]. Multiple emissions in green spectral region originate from V_o and Zn_i derived defect states[60-63] Deep acceptor states associated with mainly V_{Zn} are responsible for yellow emission[64-65]. The recombination of electron from donor state Zn_i with the deep trap states[58] may also generate yellow emission. The enhancement of emission in yellow region and decrease of emission in green region is due to the formation of more V_{Zn} with increase of Ga concentration.

The time-resolved luminescence study is essential to under-stand the origin of the different emission centers in the NCs. Time dependent emission spectra for all samples are depicted in Fig. 8. The decay profile of pure ZnO can be fitted well with bi-exponential function, where the fast decay component τ_1 = 0.93 ns and slower component τ_2 = 4.93 ns. The fast decay component is for excitonic recombination and slower one is for recombination of electron with the deep trap states corresponding to vacancies and defects. The decay components and the average lifetime of the pure and doped samples are shown in Table 3, which clearly indicate the increase in average life time of the samples upon Ga^{3+} doping. All the samples needed hundred of nanoseconds for complete deactivation, indicating deep trap nature of the defect states. The decay profile of low doping (x = 0.0025 – 0.02) and the highest doping (x = 0.04) NC was fitted with three and four exponential components respectively. This clearly suggests that multiple recombination channels are involved in Ga doped samples. Various defect levels are responsible for such recombination path ways.

Electrical Properties:

We have measured the sheet resistance of the pure and doped thin film samples in the temperature range 80 K – 300 K by conventional two probe method. The crystal structure of annealed thin films is identical with as synthesized samples which is confirmed from XRD patterns of films [Fig. S6]. Continuous deposition of film and presence of nanocrystals in as deposited and annealed film have been verified from SEM images. [Fig.S7 and Fig S8 respectively]. The annealed film shows characteristic absorption in UV-VIS-NIR region [Fig. S9]. At room temperature the sheet resistance of pure ZnO film is found to be 60 kΩ/sq. When the system was doped (x = 0.0025) with Ga in ZnO matrix then sheet resistance decreases rapidly to 1.7 kΩ/sq. With further increasing Ga concentration sheet resistance gradually decreases viz. 1200 Ω/sq. for x = 0.005, 900 Ω/sq. for x = 0.01, 650 Ω/sq. for x = 0.02 but drastically increases to 3 kΩ/sq. for x = 0.04. For higher content of Ga, localized impurity states are formed within band gap region of ZnO due to interstitial defect which causes an increase of resistance[16]. Sheet resistance, error from current voltage curve (I-V) fitting in sheet resistance measurement in room temperature and thickness of all samples are shown in Table 4. Fig S10 shows the room temperature sheet resistance with error bars for same compositional and conditional different films. The lowest achieved sheet resistance of 650 Ω/sq. in the present study is about two times higher than the recent published results (390 Ω/sq.). In later case, hydrogen and UV treatments improve the sheet resistance of Ga doped ZnO nanocrystals.[30] Sheet resistance depends on the thickness of film. Resistivity of film is more convenient to compare with earlier reported values. Resistivity as displayed in Table 4 has been calculated based on the measured thickness and the best value of resistivity for x = 0.02 is one order of magnitude lower than sol-gel derived films[66-68]. The minimum resistivity of 1.86×10^{-4} Ω.cm as shown in Table 4 is comparable to Ga doped films (3.6×10^{-4} Ω.cm) prepared by metal organic

vapor deposition[69] . The absolute value of resistivity varies with the preparation technique but the trend of variation of resistivity with Ga concentration remains almost same.

Temperature dependent electrical sheet resistance measurement of pure ZnO film as depicted in Fig. 9(a). shows semiconducting behavior as confirmed from the negative value of temperature coefficient of resistance. The resistance vs. temperature as shown in Fig. 9(b)-(e). gives a clear signature of metal - semiconductor transition (MST) with the position of the minimum for doped (x = 0.0025 - 0.02) samples[70]. The transition temperature of doped film is found to vary from 200 K to 125 K with increase of Ga concentration. The conduction band of Ga doped ZnO consists of the most extended s derived states of Zn and Ga. The metallic conductivity originates from the strong overlap of delocalized s state of conduction band with the neighboring ions. Metal like conductivity above transition temperature is due to the formation of degenerate band in doped semiconductor. The variation of resistance with temperature for x = 0.4 indicates a conventional semiconductor in which the Fermi level lies within band gap region.

The incorporation of Ga into ZnO lattice introduces two major modifications: enhancement of carrier concentration and cationic disorder. The enhancement of carrier concentration improves the metallic behavior which gives rise to shifting of MST temperature towards lower temperature region. The random substitution of Ga creates a disorder in crystal potential which leads to a localization of carriers. The constructive interference of wave function of such carriers causes an increase of resistance with decrease of temperature, known as localization effect[71]. Decrease of sheet resistance and MST transition temperature suggests a transition controlled by the electrons hopping among the defects generated by Ga ions. The temperature corresponding to the minimum position at the MST could be associated to the energy required by the electron to hop from one Ga ion to another. A plot of transition

temperature vs. concentration reveals a power law kind of relation with T proportional to concentration^{m} (with m c.a. 1/6) as shown in Fig S11. The nature of resistance with temperature is analyzed in the light of phonon scattering in metallic region and backscattering in semiconducting region as given by

$$R = \frac{1}{\sigma_o + a_1 T^{p/2} + a_2 T^{1/2}} + a_3 T^2 + R_o \quad (5)$$

where σ_o is the residual conductivity, $a_1 T^{p/2} + a_2 T^{1/2}$ is the weak localization with p taking values of 3 and 2 for electron - phonon scattering and electron - electron self scattering respectively, $a_2 T^{1/2}$ corresponds to the Coulomb electron interactions renormalized by self-interference effects, $a_3 T^2$ corresponds to the high temperature thermal scattering. However, it is observed a correction term R_o has to be added in order to obtain a good fit to the curve. The fitted plot of sheet resistance and fitting parameters are presented in Fig. 9 and Table 5 respectively. Mathematically R_0 corresponds to a shift in the origin in the high temperature contribution. A meaningful fit (with the standard errors less than the derived parameter) is obtained when the value of σ_o is set to 0. According to Matthiessen's rule resistance arising from different scattering centers when acting simultaneously, may be approximated as if they are connected in series. A negative value of R_o suggests that not all mobile electrons participating in the high temperature scattering process are contributing to the weakly localized conduction process at low temperature. This might occur either due to a phase transformation involving an accelerated generation of thermal electrons or discontinuities occurring in the material leading to parallel channels of preferred conducting region. This is also indicated by the increased values of the exponent p which represents an increased thermal dependence of relaxation time due to multiple scattering and self interference probably from the boundaries of these preferred

channels. The contribution of Coulomb electron interaction is found to change sign at higher concentration of Ga (x > 0.01).

Since the values of p > 3 are not defined in literature an attempt was carried out by replacing the term $a_1 T^{p}/_2$ by $a_4 T^{3}/_2 + a_1 T^{p}/_2$ in the spirit of Matthiessen's rule[72]. The fitted plot using $a_1 T^{p}/_2$ by $a_4 T^{3}/_2 + a_1 T^{p}/_2$ and fitted parameter showed in Fig. S12 and Table S1 respectively. It is found indeed that the data could be fitted to system with parameter p such that p lies around 2 and 3. The value of a_4 is found to be negative suggesting that the system can be explained by two competing contributions of phonon scattering (however the quality of the fit is deteriorated as observed from the values of regression coefficients). For doping concentration x >= 0.02 the fitted value of a_3 goes to 0 with the value of p closer to 3 suggesting a single kind of phonon scattering getting involved in the conduction process. Hence, it may be suggested that a combination of scattering and percolation processes control the conduction mechanism in such system.

Conclusion

The replacement of Zn by Ga modifies morphology from hexagonal nanopyramid to nanocrystals and reduces size from 39 nm to 18 nm. Higher electronegativity of Ga^{3+} and larger compressive strain control the growth kinetics. Optical band gap increases with Ga concentration due to fill up the bottom of conduction band of host ZnO. Many body effects give rise to reduction in band gap in heavily Ga doped system. Surface plasmon absorption in the infrared region originates from the spontaneous formation of high carrier concentration introduced by defects and Ga impurity. Quantitative analysis of PL spectrum suggests that the cooperative emission of multiple colors in the visible region arises from various defect derived intermediate

energy levels. Carrier concentration, modification of electronic energy band structure and disorder drive dopant and temperature induced metal - semiconductor transition. The co-existence of high optical transparency, plasmon absorption, tunable emission in the visible region and high electrical conductivity may be useful for the fabrication of multifunctional nanoscale devices.

Acknowledgement

The authors Manas Saha and Sirshendu Ghosh are thankful to Council of Scientific and Industrial Research (CSIR), Govt. of India for providing the fellowship during the tenure of the work.

Table 1: Ga concentration of $Zn_{1-x}Ga_xO$ samples based on atomic absorption spectrum analysis.

Sample ($Zn_{1-x}Ga_xO$)	**Ga precursor (mol%)**	**Ga in $Zn_{1-x}Ga_xO$ (mol%)**
x=0.0	0	0
x=0.0025	0.25	0.172
x=0.005	0.5	0.4192
x=0.01	1.0	1.89
x=0.02	2.0	3.24
X=0.04	4.0	4.91

Table 2: Optical band gap energy (E_g), plasmon wavelength (λ_p), carrier concentration (N) calculated from the Burstein-Moss effect and Mie's theory for pure and doped samples ($Zn_{1-x}Ga_xO$).

Sample	λ_P (nm)	E_g (eV)	**Mie's Theory** $N[cm^{-3}]x10^{19}$	**Burstein-Moss effect** $N[cm^{-3}]x10^{19}$
x=0.00	_	3.302	_	_
x=0.0025	6929.11	3.332	4.332	0.562
x=0.005	5893.27	3.350	5.988	0.629
x=0.01	5398.06	3.358	7.138	1.037
x=0.02	4273.04	3.407	11.392	1.094
x=0.04	4843.37	3.314	8.866	0.486

Table:3 The photoluminescence decay components (τ) and the average lifetime of the pure and doped samples ($Zn_{1-x}Ga_xO$) at emission wavelength (λ_{ems})**.**

Sample	λ_{ems} (nm)	τ (ns)				Average lifetime (ns)
		τ_1	τ_2	τ_3	τ_4	
x=0.00	492	0.93	4.93	-	-	1.03
x=0.0025	500	2.20	2.27	206.00	-	1.56
x=0.005	512	0.29	1.09	12.89	-	1.65
x=0.01	530	0.59	1.35	16.12	-	2.17
x=0.02	533	0.01	0.54	22.61	-	2.68
x=0.04	535	0.13	1.11	8.51	45.39	5.39

Table 4: Sheet resistance, thickness and resistivity of $Zn_{1-x}Ga_xO$ samples

Sample ($Zn_{1-x}Ga_xO$)	**Sheet resistance(R_s) (Error to the last significant digit from I-V fitting) Ω/sq.**	**Thickness(t) (nm)**	**Resistivity (ρ) $\times 10^{-4}$ (ohm-cm)**
x=0.0	60,000 (64)	303	16875.80
x=0.0025	1700 (8)	330	525.93
x=0.005	1200 (3)	287	3.22
x=0.01	900 (3)	293	2.50
x=0.02	650 (3)	310	1.86
x=0.04	3000 (2)	297	8.24

Table:5 Fitting parameters a_1, a_2, a_3, p and R_0 of pure and doped ZnO ($Zn_{1-x}Ga_xO$) as described in Eq.(5). σ_o is deliberately set to 0. The error to the last significant digit is given in the parenthesis.

Sample	a1	p	a2	a3	R_0(in ohms)	Adj R
x=0.00	1.82(4) x 10^{-14}	7.7(6)	3.4(1) x 10^{-8}	-0.3(1)	67352(7000)	0.99941
x=0.0025	4.3(2) x 10^{-18}	12(1)	3.62(9) x 10^{-5}	0.04463(1)	-2680(50)	0.99943
x=0.005	5.7(4) x 10^{-16}	9.7(9)	2.59(5) x 10^{-5}	0.0483(5)	-3984(77)	0.998
x=0.01	9(2) x 10^{-11}	6.0(2)	5.1(2) x 10^{-6}	0.035(1)	-1822(132)	0.99954
x=0.02	9.7(8) x 10^{-6}	3.00(3)	-6.50(4) x 10^{-4}	0.0106(2)	-283(13)	0.99181
x=0.04	1.7(1) x 10^{-7}	3.17(3)	-1.4(1) x 10^{-4}	0.0028(4)	-301(30)	0.99289

References:

(1) Pelton, M.; Aizpurua, J.; Bryant, G. *Laser & Photon. Rev*. **2008**, *2*, 136-159.

(2) Naik, G., V.; Shalaev, V., M.; Boltasseva, A. *Advanced Materials* **2013**, *25*, 3264-3294.

(3) Luther, J, M.; Jain, P., K.; Ewers, T.; Alivisatos, A., P. *Nature Materials* **2011,** *10*, 361-366.

(4) Özgür, Ü; Alivov, Ya., I.; Liu, C.; Teke, A; Reshchikov, M., A.; Doan, S.; Avrutin, V.; S Cho, S.-, J.; Morkoç, H. A. *J. Appl. Phys.* **2005**, *98*, 041301.

(5) Wang, Z., L. J. *Phys. Condens. Matt.* **2004**, *16*, R829-R858.

(6) Goings, J., J.; Schimpf, M., A., May, W., J.; Johns, W., R.; Gamelin, R., D.; Li, X. *J. Phys. Chem. C*. **2014**, *118*, 26584-26590.

(7) Gaspera, D., E.; Chesman, A., S., R.; Embden, J., V.; Jasieniak, J., J.. *Acs. Nano.* **2014**, 8, 9154-9163.

(8) Liang, X.; Ren, Y.; Bai., S.; Zhang, N.; Dai, X.; Wang, X.; He, H.; Jin, C.; Ye, Z.; Chen, Q.; Chen, L.; Wang, J.; Jin, Y. *Chem. Mater***. 2014**, 26, 5169-5178.

(9) Ghosh, S.; Saha, M.; Ashok, V., D.; Dalal, B; De, S., K.. *J. Phys. Chem. C*. **2015**, 119, 1180-1187.

(10) McCluskey, M., D.; Jokela, S., J. *J. Appl. Phys*. **2009**, *106*, 071101.

(11) Schmidt-Mende, L.; MacManus-Driscoll, J., L. **2007**, *10*, 40-48.

(12) Janotti, A; Walle, C, G., V, de. *Phys. Rev. B.* **2007**, *76*, 165202.

(13) Lu, J., G; Fujita, S.; Kawaharamura, T.; Nishinaka, H.; Kamada, Y.; Ohshima, T.; Ye, Z.. Z.; Zeng, Y., J.; Zhu, L., P.; He, H., P.; Zhao, B., H. *J. Appl. Phys*. **2007**, *101*, 083705.

(14) Roth, A, P.; Webb, J, B.; Williams, D, F. *Phys. Rev. B.* **1982** ,*25*, 7836-7839.

(15) Walsh, A; Silva, J, L., F., Da; Wei, Su-Huai. *Phys. Rev. B*. **2008**, *78*, 075211.

(16) Sans, J., A.; Sánchez-Royo, J., F.; Segura., A.; Tobias, G.; Canadell, E. *Phys. Rev. B*. **2009**, *79*, 195105.

(17) Nian, Q; Zhang, M, Y.: Schwartz, B, D.; Cheng, G, J*Appl. Phys. Lett*. **2014**, *104*, 201907.

(18) Bazzani, M; Neroni, A; Calzolari, A; Catellani, A. *Appl. Phys. Lett.* **2011**, *98*, 1210907.

(19) Jia, J; Takasaki, A; Oka, N; Shigesato, Y. *J. Appl. Phys*. **2012**,*112*, 013718.

(20) Vunnam, S; Ankireddy, K; Kellar, J; Cross, W. *Nanotechnology* **2014**, *25*, 195301.

(21) Buonsanti, R; Llordes, A; Aloni, S; Helms, B, A.; Milliron, D. J. **2011**, *11*,4706-4710.

(22) Ghosh, S.; Saha, M.; De, S., K. *Nanoscale* **2014**,*6*, 7039-7051.

(23) Su, J; Li, H; Huang, Y; Xing, X; Zhao, J; Zhang, Y. *Nanoscale* **2011**, *3*, 2182-2187.

(24) Zakutayed, A; Perry, N, H.; Mason, T, O.; Ginley, D, S.; Lany; S. *Appl. Phys. Lett*., **2013**,*103*, 232106.

(25) Bhosle, V.; Tiwari, A.; Narayan, J. *Appl. Phys. Lett.* **2006**, *88*, 0321406.

(26) Bhosle, V.; Tiwari, A.; Narayan, J. *J. Appl. Phys* .**2006**, *100*, 033713.

(27) Dalpian, G, M.; Chelikowsky, J, R. *Phys. Rev .Lett*. **2006**, *96*, 226802.

(28) Serier, H.; Gaudon, M.; Ménétrier, M. *Solid State sciences* **2009**, *11*, 1192-1197.

(29) Dasgupta, N, P.; Neubert, S; Lee, W; Trejo, O; Lee,J-R; Prinz, F, B. *Chem. Mat*. **2010**, *22*, 4769-4775.

(30) Gaspera, E, D; Bersani, M; Cittadini, M; Guglielmi, M; Pagani, D; Noriega, R; Mehra, S; Salleo, A; Martucci, A. *J. Am. Chem. Soc*. **2013**,*135*, 3439.

(31) Wei, H.; Li, M.; Ye, Z.; and Yang, Z. *Materials Lett*. **2011**, *65*, 427-429.

(32) Fujiwara, H; Kondo, M. *Phys. Rev. B*. **2005**, *71*, 075109.

(33) Farvid, S, S.; Wang, T; and Radovanovic, P, V.. *J. Am. Chem. Soc*. **2011**,*133*, 6711.

(34) Gonçalves, A, de, S; Lima, S, A, M, de; Davolos, M, R; Antônio, S, G; and Paiva-Santos, C, de, O. *J. Sol. State. Chem.* **2006**, *179*, 1330-1334.

(35) Ashcroft, W., N.; and Mermin, D., N.; Solid State Physics, Saunders College Publishing , Harcourt Brace College Publishers pp.76

(36) Yang, M; Sun, K; Kotov, N, A.. *J. Am. Chem. Soc.* **2010**, *132*, 1860-1871.

(37) Yang, R; Ding, Y; Wang, Z, L. *Nanoletters* **2007**, *4*, 1309-1312.

(38) Solís-Pomar, F; Martínez, E; Martínez, M, F; Pérez-Tijerina, E. *Nanoscale Res. Lett*. **2011**, *6*, 524.

(39) Dalmaschio, C, J; Ribeiro, C; Leite, E, R. *Nanoscale* **2010**, *2*, 2336-2345.

(40) Schwartz, D, A.; Norberg, N. S.; Nguyen, Q, P.; Parker, J, M.; Gamelin, D, R. *J. Am. Chem. Soc*. **2003**, 125, 13205-13217.

(41) Ghosh, S; Das, K; Sinha, G; Lahtinen, J.; De, S., K*J. Mat. Chem. C***. 2013**, *1*, 5557-5565.

(42) Houtepen, A., J.; Koole, R.; Vanmaekelbergh, D.; Meeldijk, J; Hickey, S., G. *J. Am. Chem. Soc*. **2006**, *128*, 6792-6793.

(43) Teranishi, T.; Eguchi, M.; Kanehera, M.; Gwo, S. *J.Mat. Chem*. **2011**, *21*, 10238-10242.

(44) M. Fox, Optical Properties of Solids, Oxford University Press, New York, 2001.

(45) Baer, W., S. *Phys. Rev*. **1966**, *154*, 785-789.

(46) Weiher, R., L. *Phys. Rev*. **1966**, *152*, 736-739.

(47) Gupta, V.; Mansingh, A. *J. Appl. Phys*. **1996**, *80*, 1063-1073.

(48) Ellingson, R., J.; Beard, M., C.; Johnson, J., C.; Yu, P.; Micic, O., I.; Nozik, A., J.; Shabaev, A.; Efros, A., l.. *Nano Lett*. **2005**, 5, 866-871.

(49) Banerjee, P.; Lee, W.-J.; Bae, K.-R.; Lee, S., B.; Rubloff, G.,W.. *J.Appl. Phys*. **2010**, *108*, 043504.

(50) Kim, K., J.; Park, Y., R. *Appl. Phys. Lett*. **2001**, *78*, 475-477.

(51) Sernelius, B., E.; Berggren, K.-F.; Jin, Z.-C.; Hamberg, I.; Granqvist, C., G. *Phys. Rev. B* . **1988**, *37*, 10244-10248.

(52) Berggren, K.-F.; Sernelius, B., E. *Phys.Rev. B*. **1981**, *24*, 1971-1986.

(53) Zhang, S., B.; Wei, S.-H.; Zunger, A. *Phys. Rev. B*. **2001**, *63*, 075205.

(54) Look, D., C.; Farlow, G., C.; Reunchan, P.; Limpijumnong, S.; Zhang, S., B.; Nordlund. K. *Phys. Rev. Lett*. **2005**, *95*, 225502.

(55) Look, D., C.; Hemsky, J., W. Residual Native Shallow Donor in Zno. *Phys. Rev. Lett*. **1999**, *82*, 2552-2555.

(56) Look, D., C.; Leedy, K., D.; Vines, L.; Svensson, B., G.; Zubiaga, A.; Tuomisto, F.; Doutt, D., R.; Brillson, L., J. *Phys. Rev. B*. **2011**, *84*, 115202.

(57) Demchenko, D., O.; Earles, B.; Liu, H., Y.; Avrutin, V.; Izyumskaya, N.; Özgür, Ü., Morkoç, H. *Phys. Rev. B*. **2011**, *84*, 075201.

(58) Zeng, B., H.; Duan, G.; Li, Y.; Yang, S.; Xu, X.; Cai, W. *Adv. Fun. Mat*. **2010**, *20*, 561-572.

(59) Zeng, H.; Li, Z.; Cai, W.; Cao, B.; Liu, P.; Yang, S. *J. Phys. Chem. B*. **2007**, *111*, 14311-14317.

(60) Omari, M.; Gupta, A.; Kouklin, N. *J. Appl. Phys*. **2010**, *108*, 024315.

(61) Li, M.; Xing, G.; Xing, G.; Wu, B.; Wu, T.; Zhang, X.; Sum, T., C.. *Phys. Rev. B*. **2013**, *87*, 115309.

(62) Ton-That, C.; Weston, L.; Phillips, M., R.. *Phys. Rev. B.* **2012**, *86*, 115205.

(63) Janotti, A.; Walle, C., G., V.,de. *Phys. Rev. B*. **2007**, *76*, 165202.

(64) Rauch, C.; Gehlhoff, W.; Wagner, M., R., Malguth, E.; Callsen, G.; Kirste, R.; Salameh, B.; Hoffmann, A.; Polarz, S.; Aksu, Y.; Driess, M. *J. Appl. Phys*. **2010**, *107*, 024311.

(65) Tuomisto, F.; Ranki, V.; Saarinen, K.; Look, D., C.. *Phys. Rev. Lett*. **2003**, **91**, 205502.

(66) Nayak, P., K.; Yang, J.; Kim, J.; Chung, S.; Jeong, J.; Lee, C.; Hong, Y.. *J. Phys. D: Applied Physics***. 2009**, 42, 035102.

(67) Jun, M, C; Park, S, U; Koh, J, H. *Nanoscale Research Lett*. **2012**,7, 639 .

(68) Lin, K-moh.; Chen, Yu-Yu. *J Sol-Gel Sci. Technol*. **2009**, 51, 215–221.

(69) Zhao, L., J.; Sun, W., X; Ryu, H.; Moon, B., Y. *Optical Materials*. **2011,** 33, 768–772.

(70) Nistor, M.; Gherendi, F.; Mandache, N., B.; Hebert, C.; Perriére, J.; Seiler, W. *J. Appl. Phys*. **2009**, *106*, 103710.

(71) Lee, P., A.; Ramakrishnan, T., V.. **1985**, *57*, 287.

(72) Kittel, Charles; Introduction to Solid State Physics (5^{th} Ed.) Wiley Eastern Limited. PP 171.

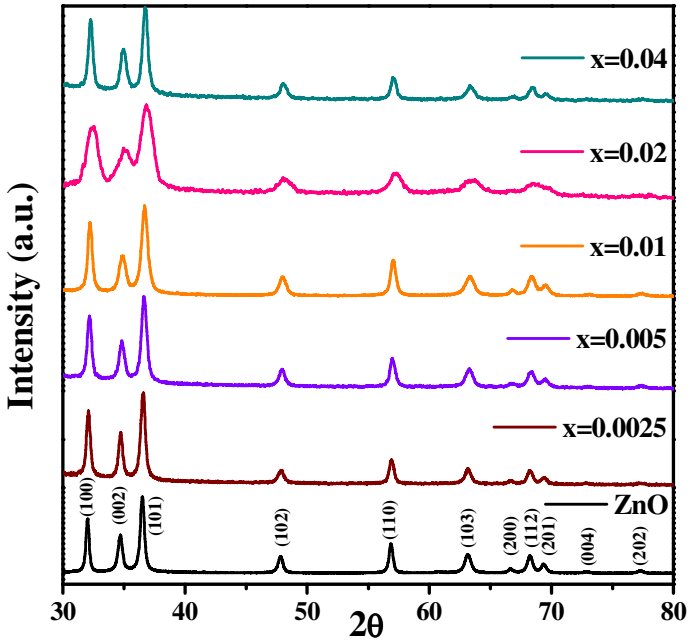

Fig.1

Fig1: XRD pattern of ZnO and doped $Zn_{1-x}Ga_xO$ nanocrystals .

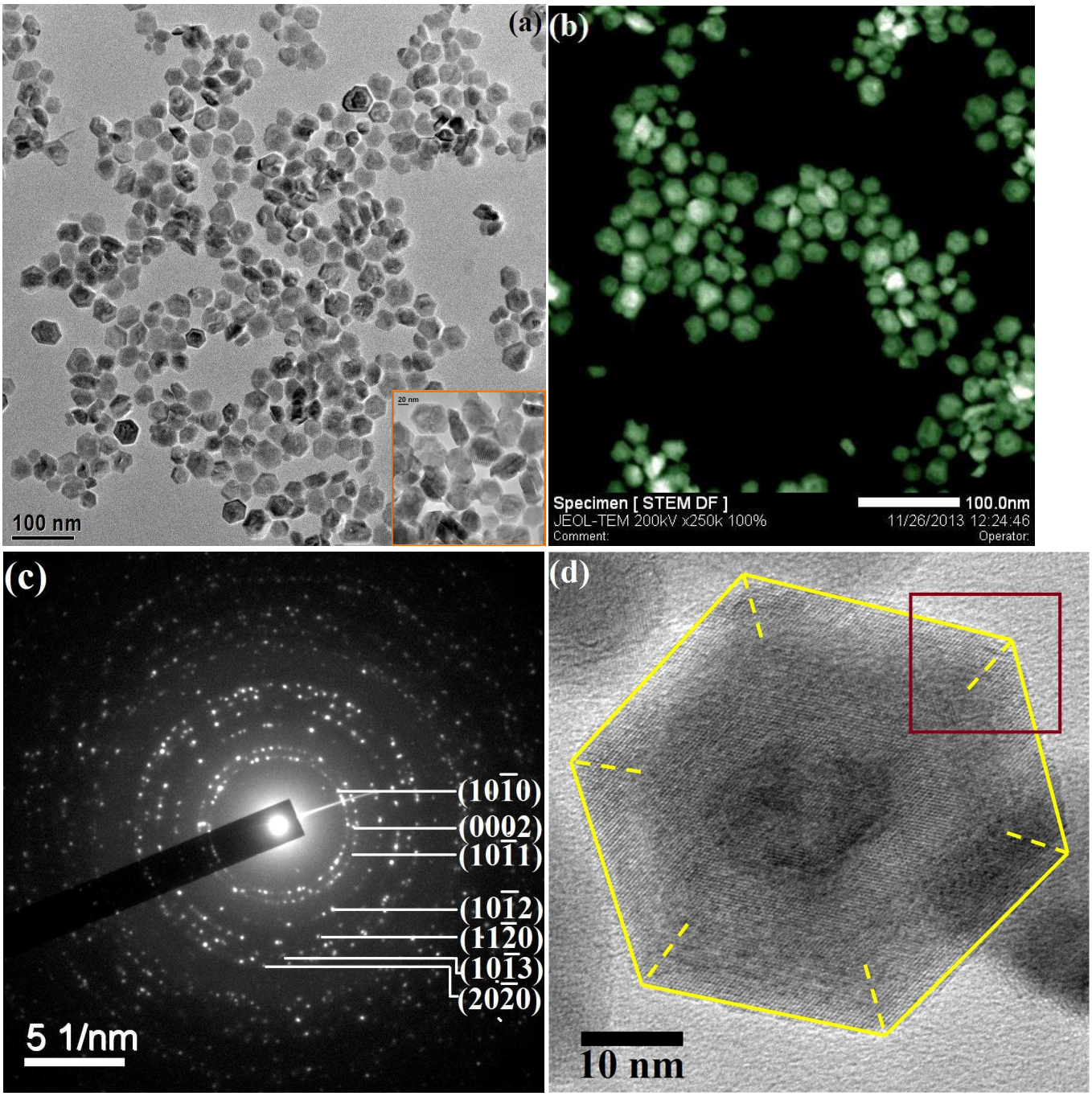

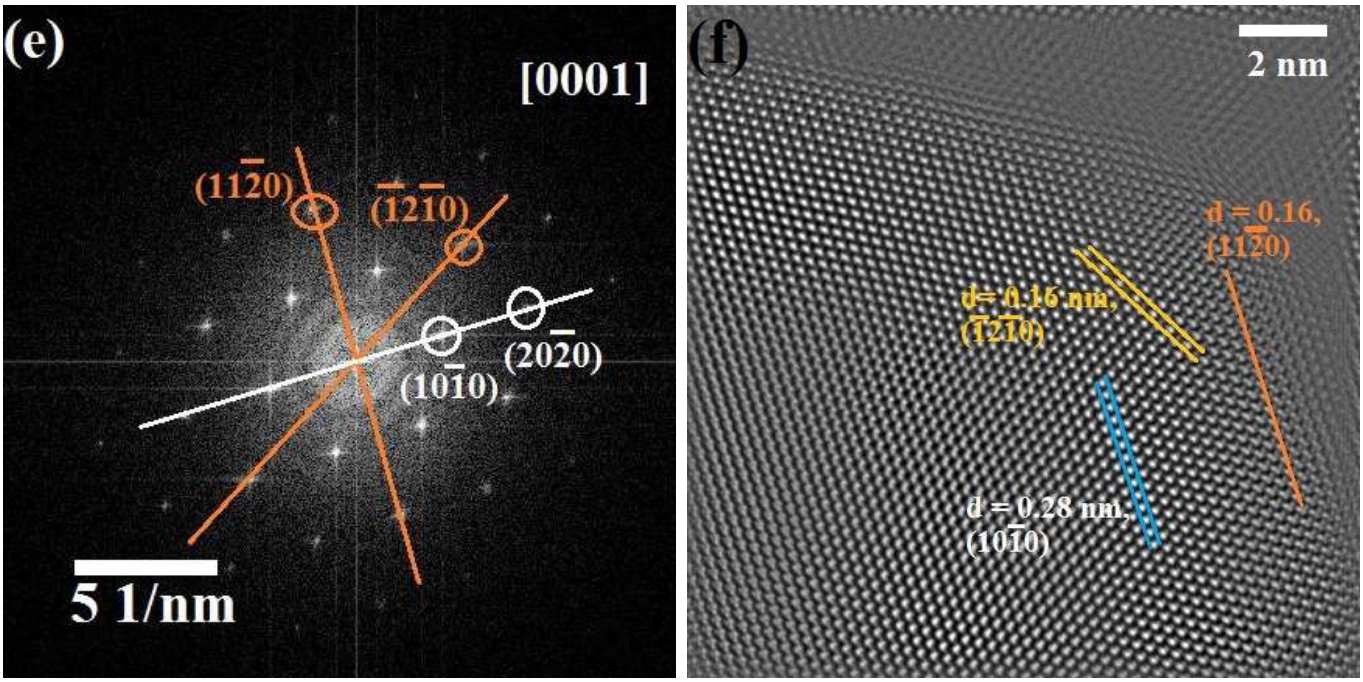

Fig. 2

Fig.2 (a) TEM image of pure ZnO nanocrystal. Inset shows tilted view of pure ZnO nanocrystals with thickness ~15-19 nm. (b) STEM dark field image of Pure ZnO. (c) SAED pattern of Pure ZnO with indexed planes. (d) HR-TEM image of a single ZnO pyramid with each side of 21 nm in length. (e) FFT pattern of colored square area of fig.2d. (f) Reconstructed TEM image from fig. 2e. The most exposed plane were indexed as (11$\bar{2}$0), ($\bar{1}$2$\bar{1}$0) and (10$\bar{1}$0).

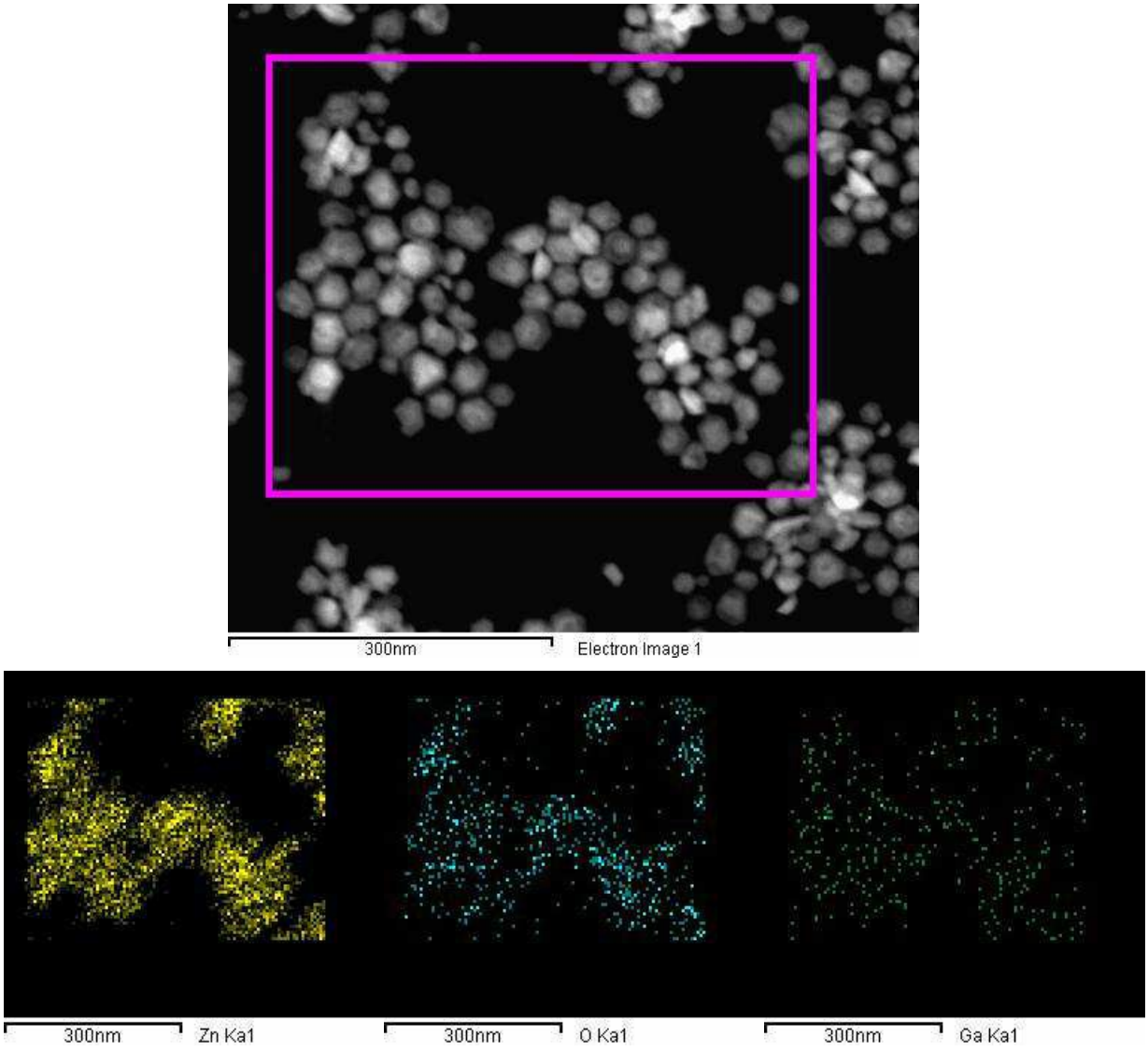

Fig. 3

Fig.3: HAADF-STEM image for $Zn_{1-x}Ga_xO$ (x=0.01) NCs. Lower Panel: EDS element mapping of the squared area for Zn, O and Ga.

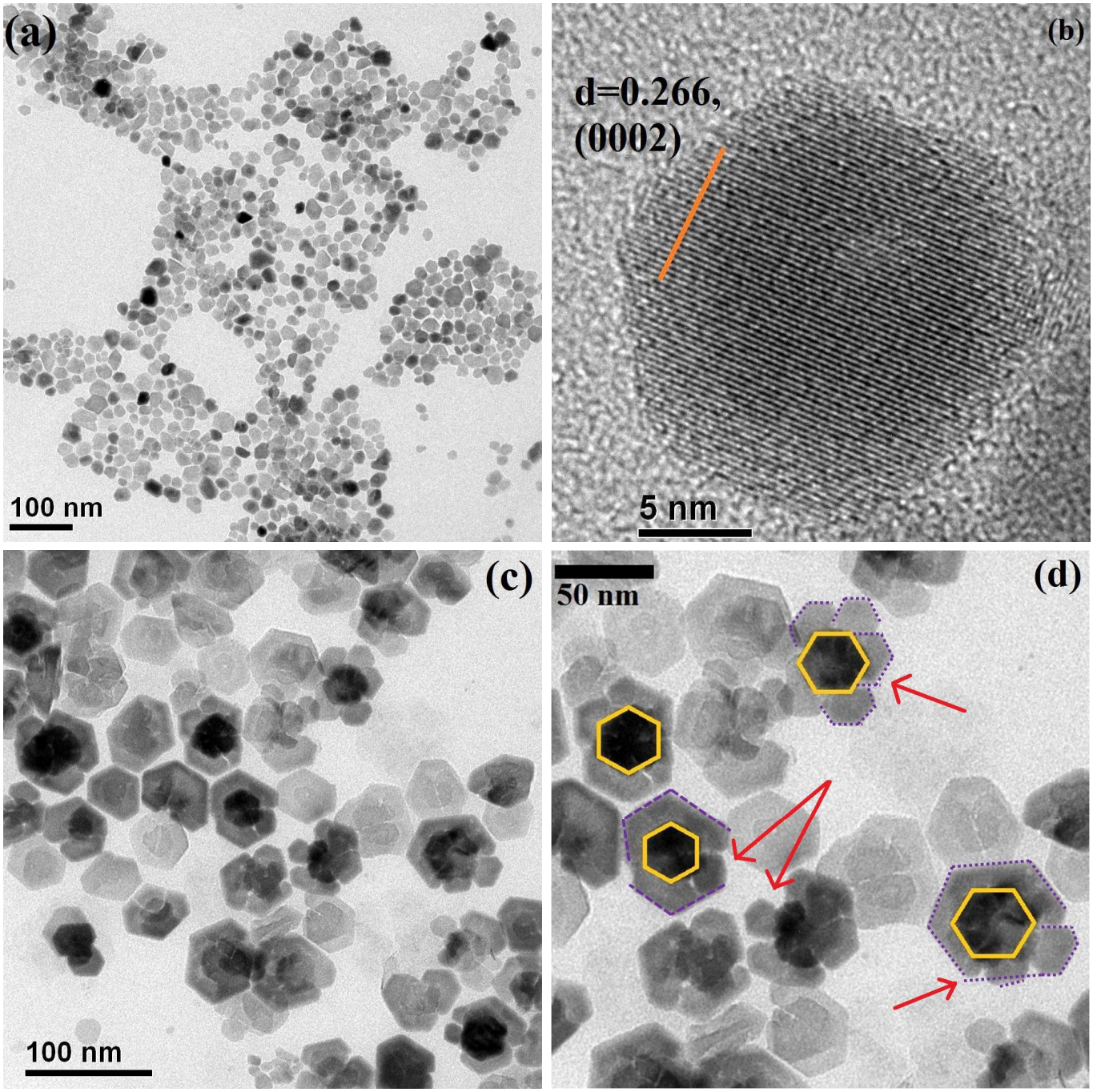

Fig. 4

Fig.4: (a) Large area TEM image for $Zn_{1-x}Ga_xO$ (x=0.02) sample. (b) HR-TEM image for x=0.02 sample shows the single crystalline nature of nanocrystal. (c) TEM image for $Zn_{1-x}Ga_xO$ (x=0.04) sample. (d) Closer view for x=0.04 sample. NCs show flower like morphology.

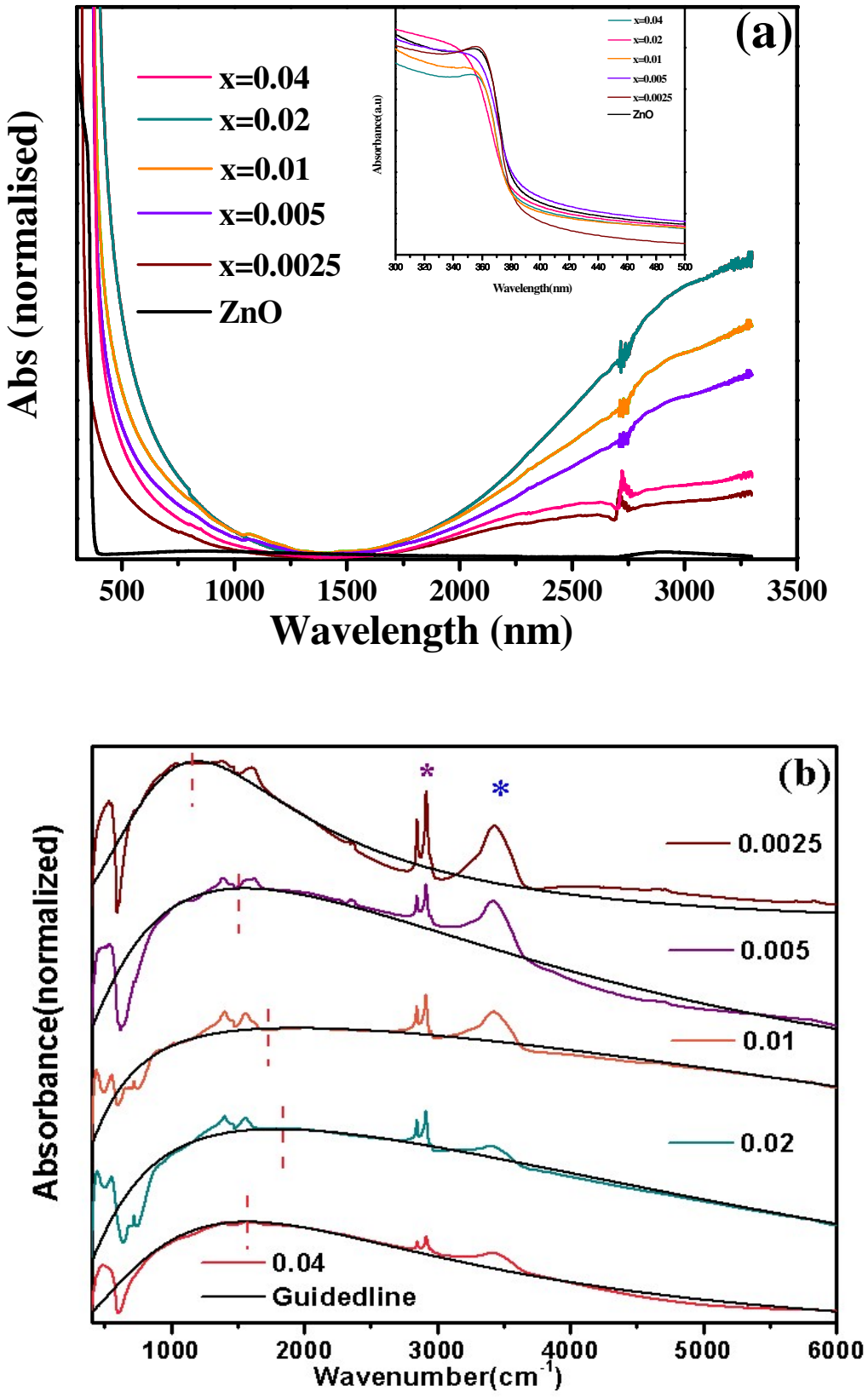

Fig.5: (a) Optical absorption spectra of pure ZnO and doped $Zn_{1-x}Ga_xO$ nanocrystals in VIS-NIR region. In set depicts band gap absorption of samples. (b) FTIR spectra of doped samples showing the plasmonic NIR absorption. Additional sharp peaks (asterisks) arise from organic ligand oleylamine absorbed on nanocrystals surface. Blue and purple asterisk represent N-H stretching and symmetric/asymmetric stretching vibration of long hydrocarbon chain respectively. Black dotted line and red vertical dotted line are guiding line for shifting of plasmonic absorption.

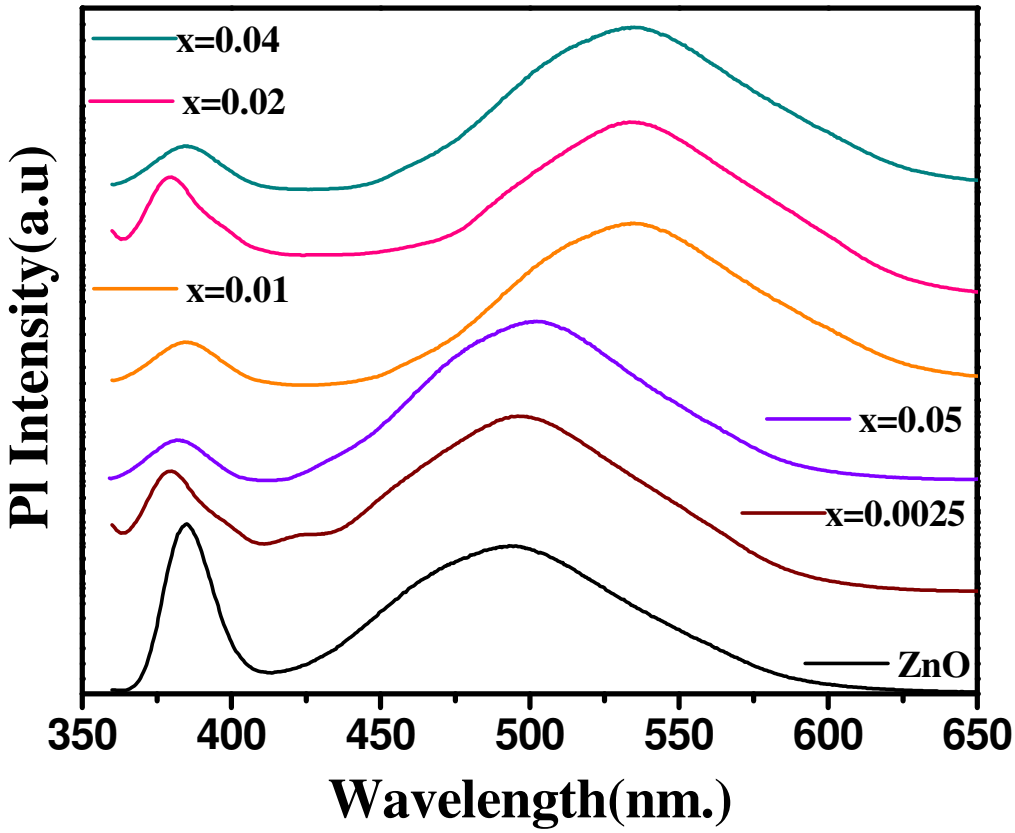

Fig. 6

Fig. 6: PL spectra of pure and doped $Zn_{1-x}Ga_xO$ nanocrystals.

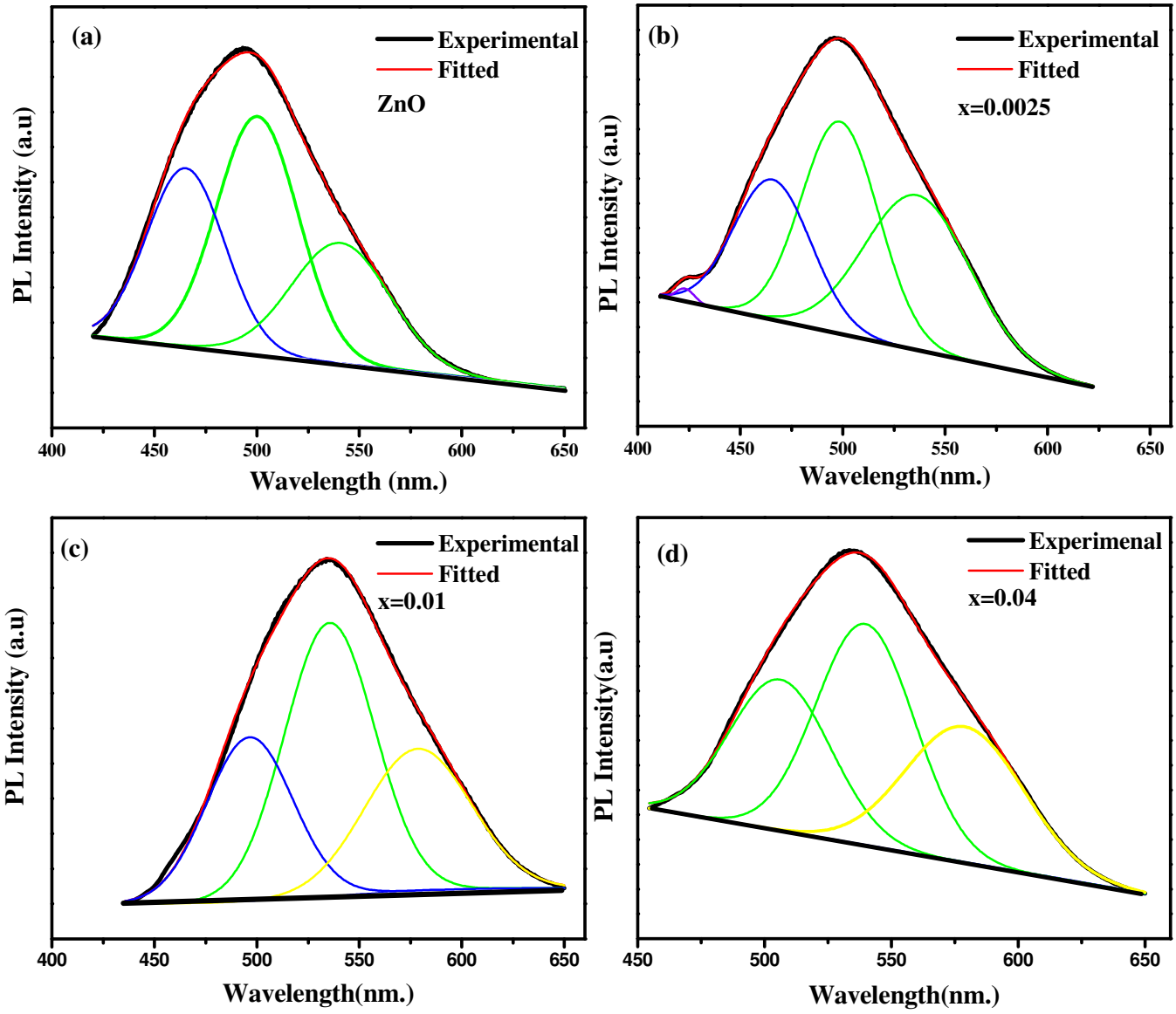

Fig.7: Deconvoluted PL spectra of (a) pure ZnO (b) x=0.0025 (c) x=0.01 and (d) x=0.04 NCs.

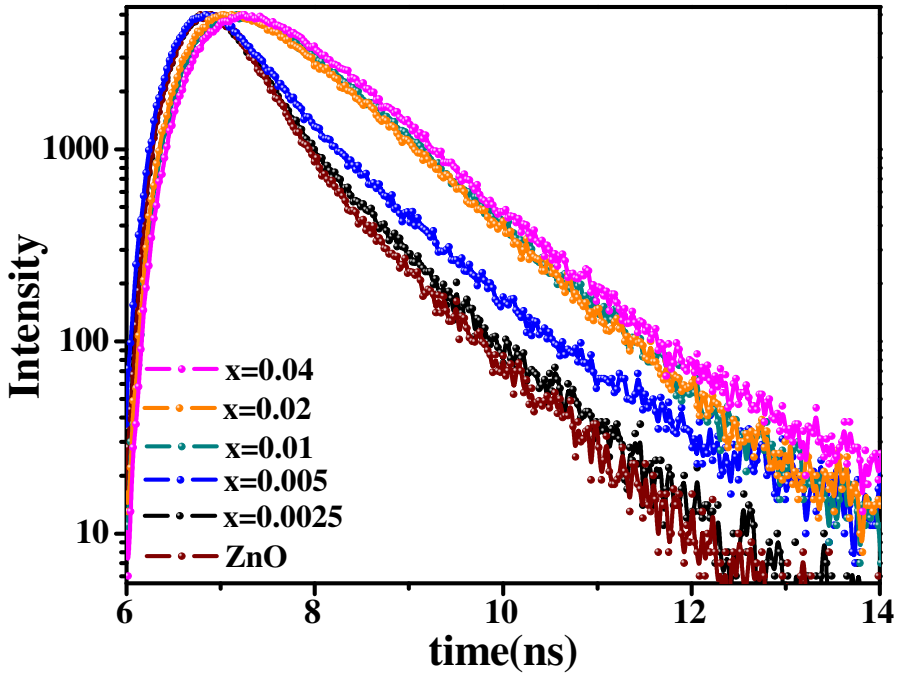

Fig. 8 Photoluminescence decays for $Zn_{1-x}Ga_xO$ with x=0.00 ($\lambda_{emission}$=495 nm), 0.0025 ($\lambda_{emission}$=505 nm), 0.005 ($\lambda_{emission}$=515 nm), 0.01 ($\lambda_{emission}$=530 nm), 0.02 and 0.04 ($\lambda_{emission}$=535 nm)

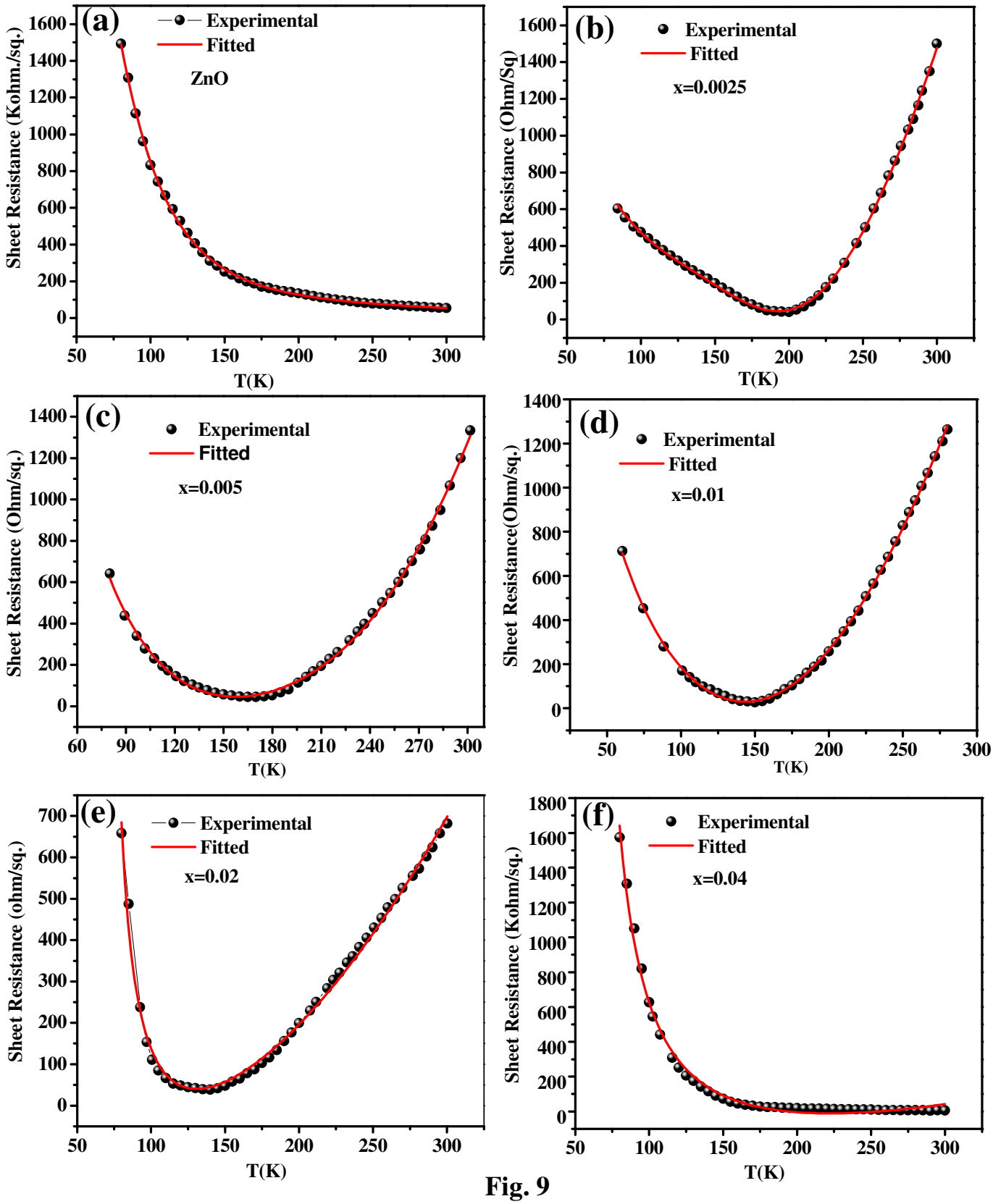

Fig. 9

Fig.9 Variation of sheet resistance with temperature for pure ZnO and $Zn_{1-x}Ga_xO$ NCs. All the data are fitted using equation:(5).